

This is a copy of the published version, or version of record, available on the publisher's website. This version does not track changes, errata, or withdrawals on the publisher's site.

Direct numerical simulation of supersonic internal flow in a model scramjet combustor under a non-reactive condition

Jian Fang, Xi Deng, and Zhi X. Chen

Published version information

Citation: J Fang, X Deng and ZX Chen. Direct numerical simulation of supersonic internal flow in a model scramjet combustor under a non-reactive condition. *Phys Fluids* 35, no. 2 (2023): 026103

DOI: [10.1063/5.0137884](https://doi.org/10.1063/5.0137884)

This article may be downloaded for personal use only. Any other use requires prior permission of the author and AIP Publishing. This article appeared as cited above.

This version is made available in accordance with publisher policies. Please cite only the published version using the reference above. This is the citation assigned by the publisher at the time of issuing the APV. Please check the publisher's website for any updates.

This item was retrieved from **ePubs**, the Open Access archive of the Science and Technology Facilities Council, UK. Please contact epublications@stfc.ac.uk or go to <http://epubs.stfc.ac.uk/> for further information and policies.

Direct numerical simulation of supersonic internal flow in a model scramjet combustor under a non-reactive condition

Cite as: Phys. Fluids **35**, 026103 (2023); <https://doi.org/10.1063/5.0137884>

Submitted: 06 December 2022 • Accepted: 19 January 2023 • Published Online: 07 February 2023

 Jian Fang,  Xi Deng and  Zhi X. Chen

COLLECTIONS

Paper published as part of the special topic on [Hypersonic Flow](#)

 This paper was selected as an Editor's Pick



View Online



Export Citation



CrossMark

ARTICLES YOU MAY BE INTERESTED IN

[Wall temperature effects on the hypersonic boundary-layer transition over an inclined, blunt cone](#)

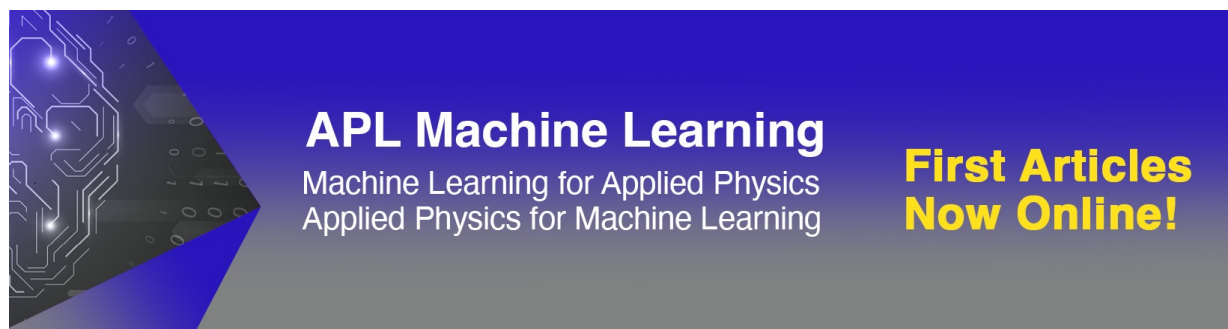
Physics of Fluids **35**, 024107 (2023); <https://doi.org/10.1063/5.0136754>

[The dynamic feedback cycle of the two-dimensional Kármán vortex street](#)

Physics of Fluids **35**, 024111 (2023); <https://doi.org/10.1063/5.0131283>

[Effects of wall disturbances on the statistics of supersonic turbulent boundary layers](#)

Physics of Fluids **35**, 025126 (2023); <https://doi.org/10.1063/5.0141369>



APL Machine Learning
Machine Learning for Applied Physics
Applied Physics for Machine Learning

**First Articles
Now Online!**

Direct numerical simulation of supersonic internal flow in a model scramjet combustor under a non-reactive condition

Cite as: Phys. Fluids **35**, 026103 (2023); doi: [10.1063/5.0137884](https://doi.org/10.1063/5.0137884)

Submitted: 6 December 2022 · Accepted: 19 January 2023 ·

Published Online: 7 February 2023



View Online



Export Citation



CrossMark

Jian Fang,¹  Xi Deng,²  and Zhi X. Chen^{3,4,a)} 

AFFILIATIONS

¹Scientific Computing Department, Science and Technology Facilities Council (STFC), Daresbury Laboratory, Warrington WA4 4AD, United Kingdom

²Department of Engineering, University of Cambridge, Trumpington Street, Cambridge CB2 1PZ, United Kingdom

³State Key Laboratory of Turbulence and Complex Systems, Aeronautics and Astronautics, College of Engineering, Peking University, Beijing 100871, People's Republic of China

⁴AI for Science Institute (AIS), Beijing 100080, People's Republic of China

Note: This paper is part of the special topic, Hypersonic Flow.

a) Author to whom correspondence should be addressed: chenzhi@pku.edu.cn

ABSTRACT

A Mach 1.5 non-reactive flow in a cavity-stabilized combustor of a model scramjet is studied via a direct-numerical simulation approach, and the analysis is focused on the interaction among boundary layer, free shear-layer above the cavity and shock wave. It is found that the impingement of the free shear-layer on the aft wall of the cavity leads to strong turbulence kinetic energy, high local pressure, and a fan of compression waves. The compression waves evolve into an oblique shock, which reflects between the upper and lower walls and interacts with the boundary layers attached to the two walls. The analysis of the turbulence production reveals that the amplification of turbulence in the core of the shear-layer and around the reattachment point is mainly due to the shear production, but the deceleration production mechanism presents a significant impact in the regions above the aft wall of the cavity and around the shock interaction points. The very low frequency commonly observed in shock wave/boundary layer interactions is not observed in the present research, which might be due to the low Reynolds number of the studied case.

Published under an exclusive license by AIP Publishing. <https://doi.org/10.1063/5.0137884>

I. INTRODUCTION

The modern air-breathing hypersonic vehicles adopt a scramjet (i.e., supersonic ramjet) as their propulsion system, whose combustor operates at a supersonic condition. Although the structure of the supersonic combustor may look relatively simple compared with a turbojet, the flow physics inside is highly complicated. Even under a cold condition (i.e., no combustion), the nonlinear interaction among boundary layer, turbulence, free shear-layer, acoustic wave, and shock-wave could lead to strongly non-equilibrium flow phenomena, which has not been well known or understood.

The cavity flame-holder was initially proposed by Roudakov *et al.*¹ as an integrated fuel injection/flame-holding approach in scramjets,² due to its good performance in the hydrocarbon combustion efficiency.^{3–5} However, the open cavity flow suffers from the oscillation of the shear-layer, which might lead to unstable combustion. As a

solution, the cavity with slanted back wall (i.e., cavity with an angled wall) was proposed.^{6,7} When the shear layer impinges on an angled wall, the acoustic wave would be deflected toward the outside of the cavity rather than the front wall, avoiding the interaction between shear-layer and acoustic wave and stabilizing the shear-layer.⁸ Therefore, many studies have been focused on the cavity flame-holder with a slanted aft wall, both experimentally and numerically. Reviews of such efforts can be found from the papers of Ben-Yakar and Hanson² and Wang *et al.*,⁹ and we will only give a brief summary of the related numerical studies.

The early numerical research of combustion was mainly based on the Reynolds-averaged Navier–Stokes (RANS) equations with chemical reactions. The cavity-stabilized combustion was conducted by Davis and Bowersox,¹⁰ and their simulations matched the experiment results. The analysis showed that the cavity flame-holders with a

slanted aft wall were able to provide flame holding for hydrocarbon scramjet applications. Kim *et al.*¹¹ analyzed the cavities with different back wall's angles, offset ratios, and length. It was confirmed from their research that the cavity was able to enhance mixing and improve combustion efficiency. Ebrahimi and Gaitonde¹² analyzed a three-dimensional (3D) scramjet with a cavity combustor using a RANS approach, and they studied the impacts of the fuel injection. Generally, RANS is able to provide an estimation of the mean flow in combustors,¹³ but the use of turbulence models brings uncertainties to the results.¹⁴ Large-eddy simulation (LES), which is able to provide much richer information than RANS, has been used to study combustion since 1990s.^{15–20} A detailed review of the applications of LES in combustion can be seen in the review paper of Pitsch²¹ in 2006. A series of studies on supersonic combustion over cavities combustors were conducted in the National University of Defence Technology, using LES²² and hybrid RANS/LES,^{23–26} and may important characteristics in the cavity-stabilized combustion were reported, such like the interaction between shear-layer and shock wave and the transport of the upstream injected fuel to the shear-layer. The hybrid RANS/LES was also adopted by Ramesh *et al.*²⁷ for the simulation of the supersonic combustion, in which a relatively large computational domain was used to include the isolator, combustor, straight section, and extender. The result of their simulation showed good agreements with experimental measurement, in terms of mean flow image and wall pressure. Zhang *et al.*²⁸ applied LES to study the cavity combustor with liquid fuel (kerosene) injected. Their analysis showed that the low-speed circulating flow inside the cavity could sufficiently atomize and evaporate the liquid fuel, and the flame is efficiently held by the cavity. Sitaraman *et al.*²⁹ conducted a numerical simulation of a cavity-based supersonic combustor, with a fuel injection from the bottom wall of the cavity. Their result clearly showed the shock wave was reflected from the slanted aft wall to the upper wall. Based on the adaptive mesh refinement technology, their mesh resolution was able to approach the local Kolmogorov scale. However, the incoming flow upstream of the cavity was set to be a laminar boundary, which could be different from a practical internal flow of a scramjet.

Direct numerical simulation (DNS), which resolves all the spatial and temporal scales of turbulence, is also very popular in the combustion community. Early research activities can also be traced back to 1990s.³⁰ However, the DNS of reactive flow is much more costly than non-reactive flow, as fully resolving the scale and detailed chemistry of combustion is very expensive.³¹ Therefore, to the knowledge of the authors, published DNS works of cavity-based supersonic combustion are scarce. However, DNS of non-reactive flow over an open cavity has been reported since 1999,³² although most DNS studies were focused on the oscillating characterizations of the shear-layer³³ and the sound generation mechanisms³⁴ for the cavity with two vertical walls. The DNS of the cavity with an angled aft wall has not been found from published literature yet.

In this series of works, we are going to present the DNS study of the internal flow in a cavity-based supersonic combustor. In the present work, we first analyze the characterization of the non-reactive flow in the combustor, which stands for the cold state of the scramjet. The rest of this paper is organized as follows. The methodology and computational setup details are described in Sec. II. The simulation results are presented in Sec. III with the focus on the shear-layer and the shock wave/boundary layer interaction (SWBLI). Finally, the conclusions are summarized in Sec. IV.

II. METHODOLOGY

A. Governing equations

For the DNS of non-reactive turbulent flow, the 3D unsteady compressible Navier–Stokes (N–S) equations are numerically solved. The set of the equations is given as

$$\begin{aligned} \frac{\partial \rho}{\partial t} + \frac{\partial \rho u_i}{\partial x_i} &= 0, \\ \frac{\partial \rho u_i}{\partial t} + \frac{\partial \rho u_i u_j}{\partial x_j} - \frac{\partial p}{\partial x_i} &= \frac{\partial \sigma_{ij}}{\partial x_j}, \\ \frac{\partial \rho E}{\partial t} + \frac{\partial \rho E u_j}{\partial x_j} + p &= -\frac{\partial q_j}{\partial x_j} + \frac{\partial u_i \sigma_{ij}}{\partial x_j}, \end{aligned} \quad (1)$$

where the primary variables are the density ρ , the pressure p , the velocity component u_i , and the total energy per unit mass E . The spatial coordinates in the streamwise, wall-normal, and spanwise directions are represented as $x_i = (x_1, x_2, x_3) = (x, y, z)$, and the corresponding velocity components are $u_i = (u_1, u_2, u_3) = (u, v, w)$. The total energy, $E = \frac{p}{(\gamma-1)\rho} + \frac{1}{2} u_i u_i$, is the sum of internal and kinetic energies, where the ratio of specific heats is given as $\gamma = 1.4$. The temporal coordinate is denoted as t .

Based on a Newtonian fluid, the viscous stress tensor, σ_{ij} , is linearly related to the strain rate as $\sigma_{ij} = \mu \left(\frac{\partial u_i}{\partial x_j} + \frac{\partial u_j}{\partial x_i} \right) - \frac{2}{3} \mu \frac{\partial u_k}{\partial x_k} \delta_{ij}$, where the dynamic viscosity, μ , is calculated based on the local temperature, T , using the Sutherland law as, $\mu = C_1 T^{1.5} / (T_S + T)$, with the coefficient $C_1 = 1.458 \times 10^{-6} \text{ kg}/(\text{ms}\sqrt{\text{K}})$ and the Sutherland temperature, $T_S = 110.4 \text{ K}$. The heat flux vector, q_i , is calculated according to the Fourier's law as, $q_i = -\lambda \frac{\partial T}{\partial x_i}$, where $\lambda = \mu C_p / \text{Pr}$ is the coefficient of thermal conductivity, $\text{Pr} = 0.72$ is the Prandtl number, and $C_p = \gamma R / (\gamma - 1)$ is the specific heat capacity of the gas at constant pressure with the gas constant, $R = 287.1 \text{ J}/(\text{K kg})$.

B. Numerical method

By using the Jacobian transformation and conformal mapping, Eq. (1) is projected to a computational domain to deal with a local mesh deformation, and the transformed N–S equations are solved within a framework of high-order finite difference method. A high-order computational fluid dynamics (CFD) code, ASTR, which has been applied to DNS and LES of a series of high-speed flows,^{35–38} is adopted as the CFD solver. The convection terms of Eq. (1) are solved with a seventh-order low-dissipative monotonicity-preserving (MP7-LD) scheme,³⁹ which can resolve small-scale turbulent structures as effectively as high-order central schemes, while preserving monotonicity near shock waves. The diffusion terms in Eq. (1) are solved using a sixth-order central scheme. After all the spatial terms are solved, a three-step third-order total variation diminishing Runge–Kutta method, proposed by Gottlieb and Shu,⁴⁰ is used for the temporal integration, due to its good performance in preserving the monotonicity near discontinuities. This temporal integration scheme has also been used in our previous DNS and LES of SWBLI flows.^{35–39}

C. Flow condition, computational domain, and mesh

The flow condition and computational domain are set by referencing a series of studies on the dual-mode, direct-connect

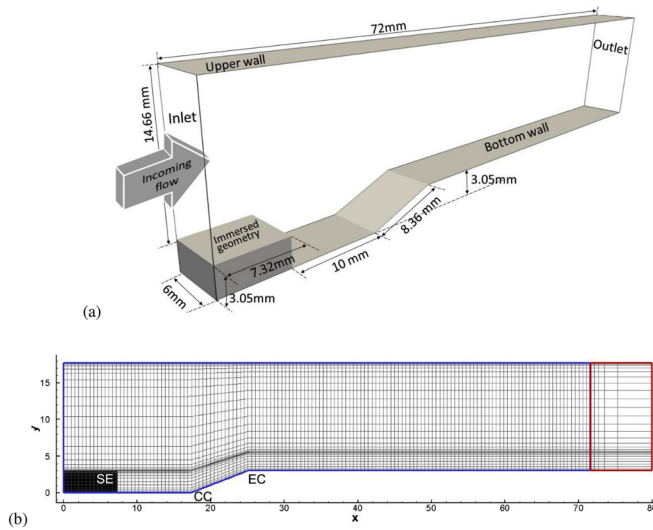


FIG. 1. Sketch of the computational domain (a) and the mesh in a x - y plane (b). The mesh nodes are drawn every ten nodes in the both directions for a better visualization, and the blue and red outlines represent the effective domain and the sponge layer, respectively. SE, CC, and EC represent the edge of the step, the compression corner, and the expansion corner of the aft wall.

combustor at the University of Virginia Supersonic Combustion Facility,^{41–44} especially the recent numerical simulations of Sitaraman *et al.*²⁹ and Johnson *et al.*⁴⁵ The computational domain is basically a quasi-3D planar channel with a cavity embedded in the bottom wall, as shown in Fig. 1. The cavity has a vertical front wall and a slanted aft wall with a 24° deflection angle. The length of the effective computational domain is 72 mm as shown in Fig. 1(a), and a sponge layer is attached to the end of the effective domain as shown in Fig. 1(b). The overall length of the computational domain is 80 mm. The incoming freestream fluid is air at 50 060 Pa and 1000 K. The mainstream flow speed is $u_\infty = 951$ m/s, and the corresponding Mach number is 1.5. The boundary layers attached on the both upper and bottom walls are assumed to be fully developed turbulent at the inlet plane. The nominal thickness of the boundary layer is $\delta_0 = 1.47$ mm, and the corresponding Reynolds number is $Re_{\delta_0} = 5871$.

The computational domain is discretized with a $1450 \times 320 \times 200$ mesh in the streamwise, wall-normal, and spanwise directions, respectively, of which $50 \times 320 \times 200$ nodes are used in the sponge layer. The mesh is basically uniformly distributed in the x and z directions in the effective domain and concentrated toward the walls in the wall-normal direction. In the sponge layer, the mesh is highly stretched toward the outlet in the streamwise direction for the purpose of damping fluctuations, as shown in Fig. 1(b). Near the two corners of the cavity's aft wall, the mesh is smoothly deformed to fit the change of the geometry, and an immersed

boundary method is used to mask the mesh upstream of the cavity [shown as the black block in Fig. 1(b)] so that a single block mesh can be used. The mesh near the surface of the immersed geometry is also refined to the same solution as that at the walls. The detailed information of the mesh resolution at the inlet plane is listed in Table I, from which we shall note that a very fine mesh is used in the present study according to the resolution criterion for wall-bounded turbulence suggested by Sagaut.⁴⁶ The ratio between the mesh spacings and the local Kolmogorov length scale, η , is estimated *a posteriori*, and the ratios at the wall and the edge of the boundary layer are listed in the table. We can confirm that the mesh resolution used in the present DNS reaches the Kolmogorov scale in the undisturbed boundary layer.

The time step for the simulation is set as $\Delta t = 2.1$ ns, and corresponding Courant–Friedrichs–Lewy number is around 0.8. The simulation is conducted until $t = 1.86$ ms. The samples are collected every 500 steps starting from $t = 0.6$ ms, and a total number of 1200 samples are collected for analysis.

D. Boundary conditions

The computational domain is positioned in a fully turbulent flow, and a proper turbulence inflow condition is therefore required. Although many inflow turbulence generation methods have been proposed for this issue, such as the rescale–reintroduction method and the digital filter (see Ref. 47 for a detailed review), they both need a transitional zone of at least ten times of the boundary layer thickness to let the fluctuations evolve. In the present study, we conducted an auxiliary DNS of a supersonic turbulent boundary layer under the same Mach and Reynolds numbers, in which a steady wall blowing and suction are used to trigger a boundary layer transition. A temporal sequence of flow slices was extracted and saved from the fully developed turbulent zone as the inflow turbulence. The inflow turbulence is further decomposed into mean flow and fluctuations as, $f(y, z, t) = \bar{f}(y) + f'(y, z, t)$, where the overbar, $\bar{\cdot}$, stands for a Reynolds-averaged variable and the quotation mark, $'$, stands for the fluctuation from the Reynolds averaging. The mean boundary layer profiles are applied to the boundary layers attached to the both upper and bottom walls, and channel flow like profiles are then obtained and prescribed at the inlet plane, as shown in Fig. 2(a). The fluctuations from two different instants with the time interval $t_{sep} = 1.4$ ms (the nondimensional value is $427.55\delta_0/u_\infty$) are, respectively, mapped to the bottom and upper boundary layers as sketched in Figs. 2(b) and 2(c). The time interval, t_{sep} , is long enough to ensure the fluctuations in the upper and lower boundary layers to be uncorrelated. The generated inflow data are applied at the inflow plane with a supersonic inflow boundary condition, except for the subsonic portion of the boundary layer, where the subsonic inflow condition proposed by Rudy and Strikwerda⁴⁸ is used. The inflow fluctuations are updated with the simulation, and a cubic spline interpolation is adopted to interpolate fluctuations in time.

TABLE I. Mesh resolution at the inflow plane. The subscript, 1, represents the value at the first node away from the wall including the surface of the immersed geometry, and the subscript, e, stands for the value at the edge of the boundary layer. The effective mesh spacing is defined as $\Delta = \sqrt[3]{\Delta x \Delta y \Delta z}$.

Δx^+	$\Delta x/\eta_1$	$\Delta x/\eta_e$	Δy_1^+	$\Delta y_1/\eta_1$	Δy_e^+	$\Delta y_e/\eta_e$	Δz^+	$\Delta z/\eta_1$	$\Delta z/\eta_e$	Δ_1/η_1	Δ_e/η_e
3.07	5.40	1.49	0.48	0.42	8.91	2.33	3.60	3.17	0.88	1.93	1.45

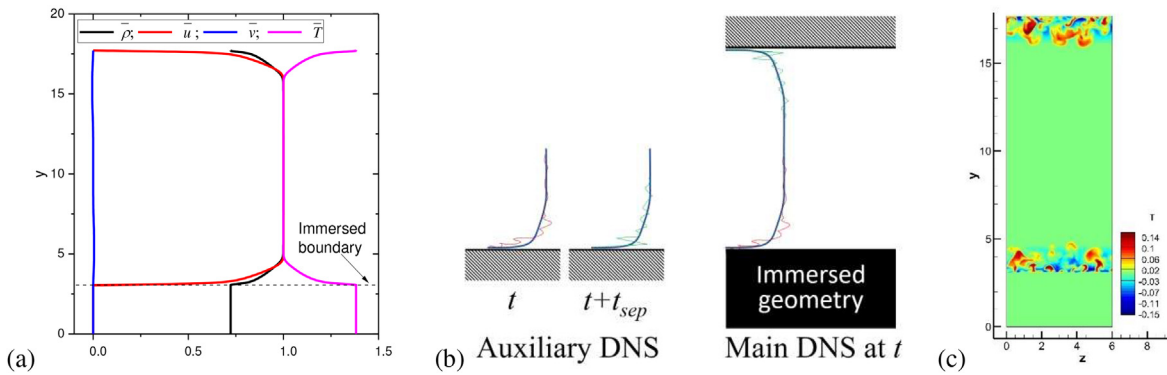


FIG. 2. Mean profiles imposed at the inlet plane (a), the schematic diagram of the interpolation of the inflow turbulence to the computational domain (b), and an instant temperature fluctuation at the inflow plane (c).

At the outlet plane, the non-reflective boundary condition⁴⁹ is applied to let all the waves go out of the computational domain. On the top and bottom walls, the adiabatic nonslip condition is applied. In the spanwise direction, the periodic condition is used on the two side boundaries.

The boundary condition for the immersed geometry needs to be addressed here. In the present study, we applied the immersed boundary method in a non-uniform mesh. The method proposed by Vanna *et al.*⁵⁰ is applied after some modifications. Nodes inside the immersed geometry that will be accessed in the calculation of fluxes on the fluid nodes are first marked as ghost nodes, as shown in Fig. 3. The image nodes are then established from the ghost nodes along the direction normal to the boundary. The flow variables on the image nodes are calculated from the nearby fluid nodes using a trilinear interpolation, and the variables on the corresponding ghost nodes are then obtained via the adiabatic nonslip condition. The ghost nodes very close to the boundary are marked as the boundary nodes, and the variables on them can be directly obtained from the specific boundary condition. For the image node that is close to the boundary, Vanna *et al.*⁵⁰ originally used a specific interpolation for cut cells. In the present study, however, we propose to extend the image node to a further distance until the trilinear interpolation can be properly done. This can be seen from the ghost-image nodes pair in the bottom right of Fig. 3.

III. RESULTS AND DISCUSSION

A. Validation

The statistics of the disturbed boundary layer upstream of the cavity ($x = 5.88$ mm) are validated against the experiments and

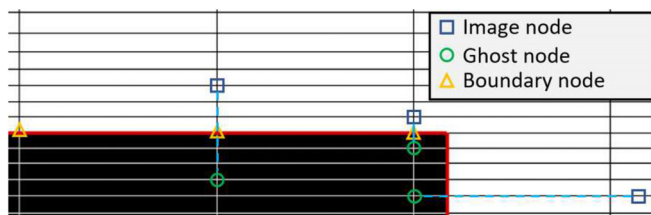


FIG. 3. Sketch of the implementation of the immersed boundary method in a non-uniform mesh. Only some representative nodes are shown briefly.

previous DNS results, and the boundary parameters at the location are listed in Table II.

The mean velocity profile, $\langle u \rangle$, is compared with the result of a Mach 2 turbulent boundary layer of Pirozzoli and Bernardini⁵¹ in Fig. 4(a), in which an excellent agreement between the results from the two DNS is obvious. Note that the operator, $\langle \cdot \rangle$, stands for a Favre-averaged variable, defined as $\langle f \rangle = \overline{\rho f} / \bar{\rho}$, which is commonly used in calculating statistics of compressible flows to avoid the appearance of density fluctuating terms. The fluctuation from the Favre averaging is denoted as, $f'' = f - \langle f \rangle$. The van Driest transformed mean velocity profile, $u_{vd} = \int_0^{(u)} \frac{\bar{\rho}}{\bar{\rho}_w} d(u)$, in the local wall unit is compared with the classic law of wall and the measurements^{52,53} as well as the DNS data of incompressible boundary layer,⁵⁴ and again, we observe a good agreement of the present DNS with the incompressible data. Note that the subscript w stands for the values at wall. This indicates the compressible effect on the mean statistics is mainly reflected by the density variation across the boundary layer, which has been confirmed up to Mach 12 by Duan *et al.*⁵⁵ The profiles of the root mean square (rms) of the velocity fluctuations and Reynolds shear stress in the undistributed boundary layer are compared with the DNS data of Pirozzoli and Bernardini⁵¹ in Fig. 5, where we can further confirm the good agreement between the results of the two DNSs.

B. Instantaneous flow

The instant field is first visualized to give an intuitive observation of the flow. The flow field on a x - y plane at an instant is shown in Fig. 6. From Figs. 6(a) and 6(b), we can see a free shear-layer form above the cavity. When the shear-layer hit the aft wall of the cavity, the local pressure is rapidly increased [Fig. 6(c)], and the compression

TABLE II. Boundary layer parameters at $x = 5.88$ mm. The symbols, δ^* and θ , stand for the displacement and momentum thicknesses for the boundary layer, and the Reynolds numbers, Re_δ , Re_{δ^*} , and Re_θ are based on the corresponding thicknesses, and the friction Reynolds number, Re_τ , is defined as, $Re_\tau = \rho_w u_\tau \delta / \mu_w$, in which u_τ is the local friction velocity.

δ	δ^*	θ	Re_δ	Re_{δ^*}	Re_θ	Re_τ
1.65 mm	0.38 mm	0.18 mm	6572	1503	705	197

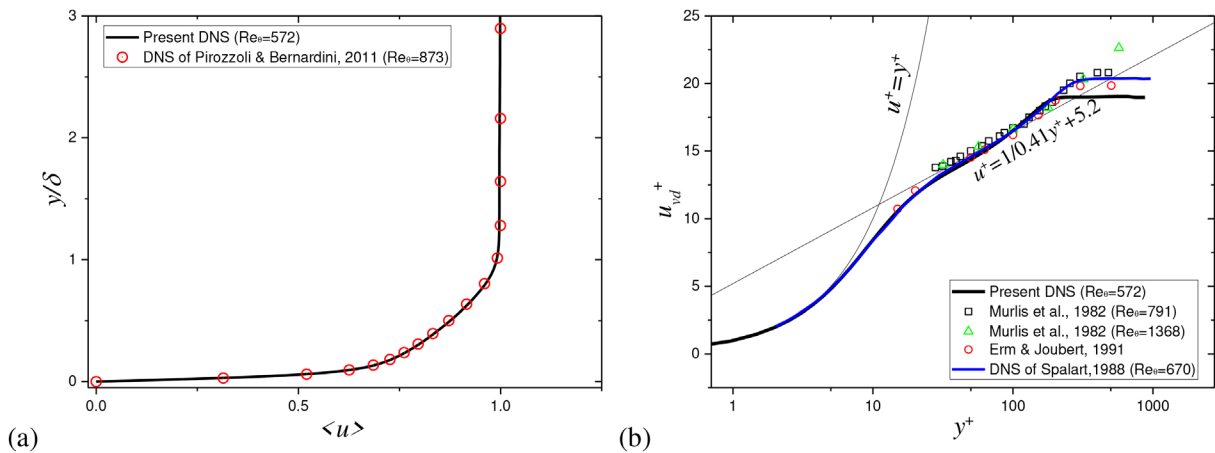


FIG. 4. Mean velocity profile at $x = 5.88$ mm in out-scaling (a) and inner scaling (b).

waves [shown as large negative values in Fig. 6(b)] are generated. The compression waves move toward the upper wall and collapse into an oblique shock-wave. The shock-wave impinges on the upper wall and leads to the first SWBLI. Afterward, the shock-wave is reflected back to the bottom wall with a relatively stronger strength, observed as the higher levels of the density gradient, $|\nabla \rho|$, and negative velocity divergence, $-\nabla \cdot \vec{u}$, in Figs. 6(a) and 6(b). The reflected shock-wave impinges on the bottom wall and causes the second SWBLI, following which the shock-wave is reflected again, but its strength is obviously weakened, observed as the decreasing values of density gradient and negative velocity divergence in Figs. 6(a) and 6(b). However, we can still observe the third SWBLI happened on the upper wall. The shock-wave is once again reflected from the upper wall, and its strength becomes even weaker. Further downstream, the shock-wave decays to compression waves, but we can still observe the reflection of the compression waves between the upper and bottom walls, as shown in Fig. 6(c). Some compression waves can also be observed between two reflected shock-waves,

which are possibly induced by the flow reattachment downstream of the interaction point.

From Figs. 6(d) and 6(e), the flow in the cavity is observed to have lower speed and higher temperature due to the circulating flow inside the cavity, which creates an ideal environment for ignition and stable combustion. Strong vortical structures with large spanwise vorticity are generated in the free shear-layer, as shown in Fig. 6(f). The swirling motion of these structures also induces local low-pressure spots, which can be observed in Fig. 6(c), as a result of the centrifugal force. From Fig. 6(f), we also note that the impingement of the shear-layer on the aft wall induces a thick layer with strong vorticity.

The turbulent coherent structures and shock-waves are visualized using the iso-surfaces of λ_{ci} criterion⁵⁶ and pressure gradient in Fig. 7. The reflection of the shock-wave between the two walls and the corresponding SWBLI can be seen in Fig. 7(a). The turbulent coherent structures present as streamwise elongated vortices upstream of the cavity, known as hairpin-like structures of wall turbulence.⁵⁶ The wall turbulence evolves into free-shear turbulence in the shear-layer above

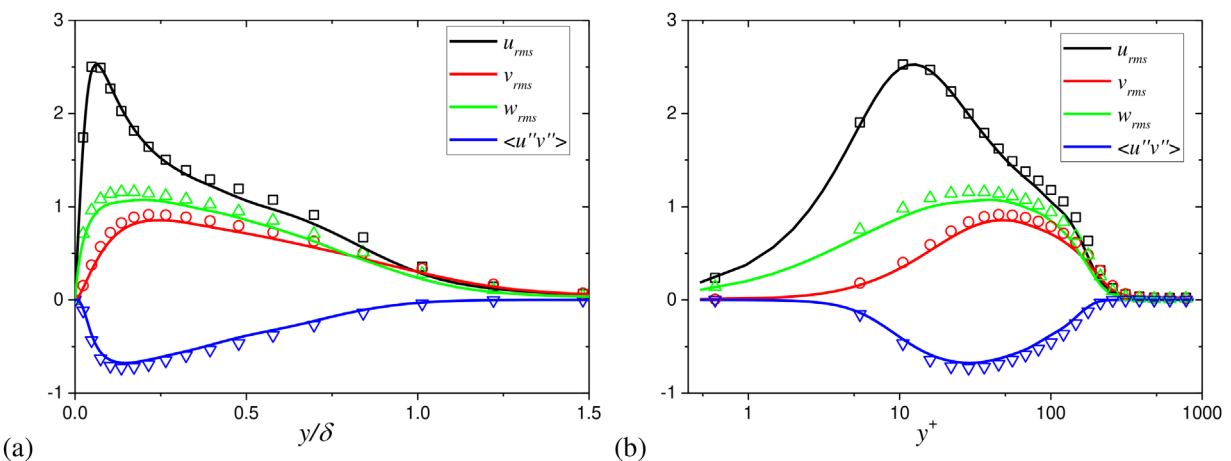


FIG. 5. The rms velocity fluctuations and Reynolds shear stress velocity profiles at $x = 5.88$ mm in out scaling (a) and inner scaling (b). The scatter results are from the DNS of a Mach 2 boundary layer by Pirozzoli and Bernardini.⁵¹

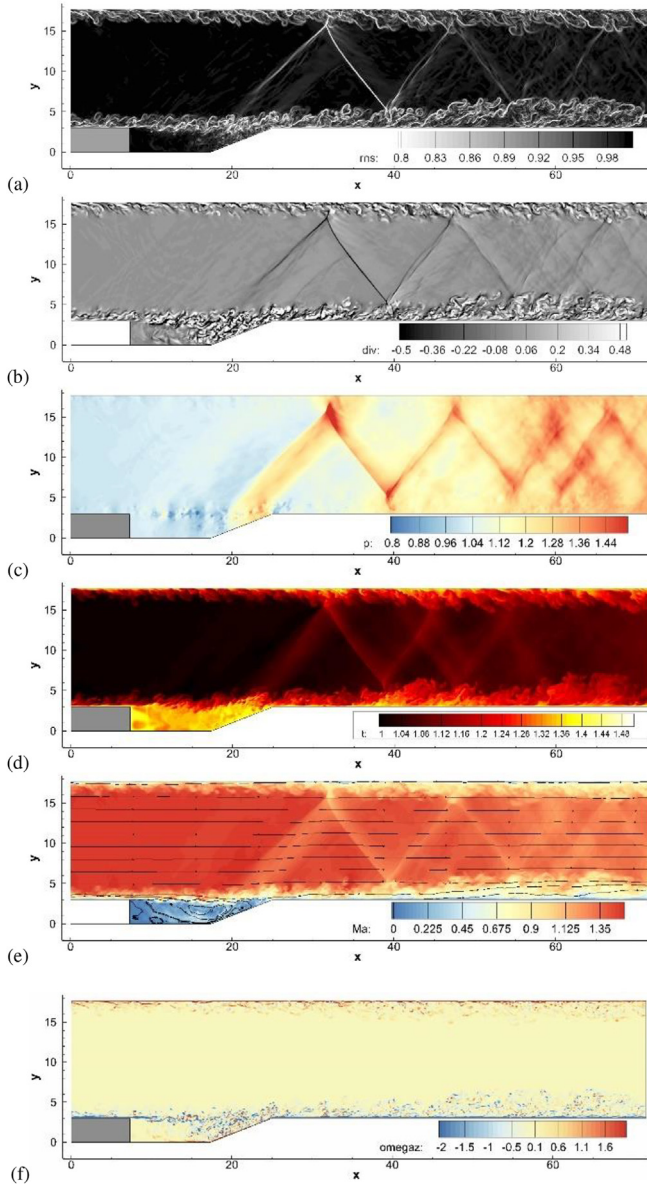


FIG. 6. Instantaneous flow field in a x - y plane. (a) Schlieren; (b) velocity divergence; (c) pressure; (d) temperature; (e) local Mach number; (f) spanwise vorticity. The schlieren (a) is calculated via the density gradient as, $rms = e^{-10 \frac{|\nabla \rho| - |\nabla \rho|_{min}}{|\nabla \rho|_{max} - |\nabla \rho|_{min}}}$ and $|\nabla \rho| = \sqrt{\frac{\partial \rho}{\partial x_i} \frac{\partial \rho}{\partial x_i}}$. The pressure and temperature are normalized with the free-stream values. The arrow lines in (e) stand for the streamlines.

the cavity, whose swirling motion is strengthened, but the anisotropy is weakened, as shown in Fig. 7(b). The impingement of the turbulence structures in the free shear-layer onto the aft wall is further visualized in Fig. 7(c), where rich turbulent structures can be seen above the aft wall. Inside the circulation zone, however, few coherent structures can be observed, which indicate the flow inside the cavity is less organized.

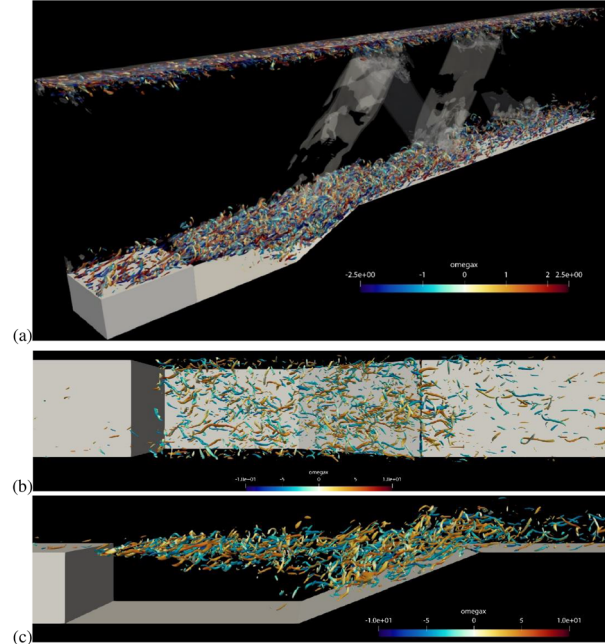


FIG. 7. The instantaneous turbulence coherent structures visualized with the λ_{cj} criterion colored with the streamwise vorticity. The shock-waves/compression-waves are visualized with the iso-surfaces of the pressure gradient, $|\nabla p|$. The coherent structures in the free shear-layer are highlighted in (b) and (c) with a larger value of the iso-surfaces of λ_{cj} .

C. Mean flow

According to the mean pressure gradient $|\nabla p|$ shown in Fig. 8(a), we can see the compression waves are generated from the shear-layer because of the impingement of the shear-layer onto the aft wall. These compression waves are focused on the point A on the upper wall and induce the first SWBLI. At the expansion corner, an expansion fan can be observed, and the pressure continuously decreases when the flow passes through the expansion fan, as shown in Fig. 8(b). The shock-wave is then reflected between upper and lower walls, and interacts with the boundary layer at points A, C and E on the upper wall and points B and D on the lower wall. On each interaction point, we can observe an expansion fan, which deflects the streamline to the wall-parallel direction and reduces the mean pressure. Consequently, the pressure is increased by shock-wave and then quickly reduced by expansion waves. Near the outlet of the computational domain, both shock-wave and expansion waves become weak, but the mean pressure has relatively higher values.

The mean temperature shown in Fig. 8(c) further confirms the high-temperature zone inside the cavity. At each interaction point, the thermal boundary layer becomes thicker. Near the outlet of the computational domain, a much thicker thermal boundary layer than the incoming flow can be observed. According to the mean local Mach number shown in Fig. 8(d), we can further confirm the thickening of the boundary layer downstream of the cavity. The flow inside the cavity presents two vortices, a primary vortex and a corner vortex, as highlighted in Fig. 8(d). This agrees with the observation of a flow over a backward-facing step.^{57,58} The local Mach number in the cavity

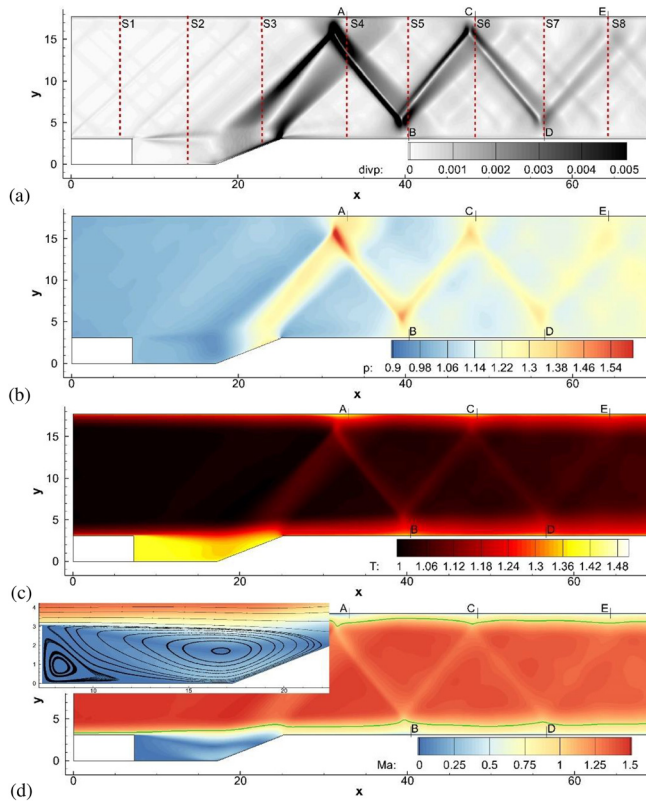


FIG. 8. The mean flow field. (a) Pressure gradient, $|\nabla p|$; (b) pressure; (c) temperature; (d) local Mach number. The pressure and temperature are normalized with the freestream values. The green lines in (d) stand for the mean sonic line, and the black lines in the zoomed subfigure are mean streamline. The interaction points on the upper and lower walls are marked with A–E, respectively. Representative stations S1–S8 for the analysis of profiles are shown in (a).

is much lower than the mainstream flow, which is favorable for ignition and combustion.

The mean wall pressure and skin-friction coefficient, C_f , on the upper and lower walls are presented in Fig. 9. From the mean wall pressure on the lower wall, we can confirm the impingement of the shear-layer on the aft wall causes a highly increased local pressure, which in turn leads to the generation of compression waves, as shown in Figs. 6(c) and 8(b). The wall pressure is then sharply reduced near the expansion corner due to the expansion fan. The minimal wall pressure is reached at the expansion corner. On the upper wall, we can note the first wall pressure peak is reached at the point A, where the first SWBLI happens, and the mean wall pressure reaches the maximal value. Following the point A, a series of wall pressure peaks are identified in the interaction zones marked with B–E in Fig. 9(a). Note that the values of these local wall pressure peaks gradually decrease in the downstream development, indicating the weakening of the strength of the SWBLI.

From the skin-friction shown in Fig. 9(b), the circulation zone in the cavity can be identified from the negative skin-friction on the lower wall. The flow separates from the edge of the step, which is a common characteristic of flow pass a backward step. The reattachment point is

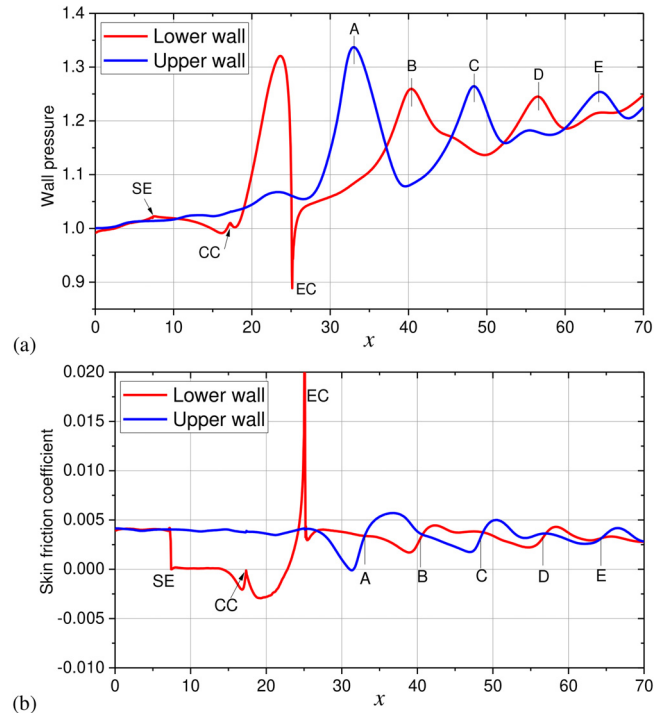


FIG. 9. Wall pressure (a) and skin-friction coefficient (b) on the lower and upper walls. The wall pressure is scaled with the freestream pressure.

identified as $C_f = 0$ on the aft wall, which is also the shear-layer impinging point, where the wall pressure gets to the maxima. Afterward, the skin-friction is rapidly increased due to the flow being accelerated by the expansion fan. Downstream the expansion corner, we note the skin-friction is constantly reduced by the shock interaction, although the locations of the local minimal C_f are ahead of the local pressure peaks due to the precompression effect of the SWBLI. For the first SWBLI around point A, the skin-friction reaches zero, meaning the local SWBLI is strong enough to trigger a local flow separation. For all other SWBLI locations, C_f maintains to be positive values due to the weaker interactions on these locations.

The time-averaged wall pressure and skin-friction lines on the two walls are shown in Fig. 10. The local high-pressure zones are identified at the points A–E, as the result of SWBLI. The wall pressure and skin-friction lines basically present a two-dimensional pattern in the most area of the walls, and three-dimensional characteristics can be observed inside the separation zone and especially near the reattachment points. The skin-friction lines on the lower wall present a typical saddle-node structure around the reattachment point, which has been widely observed in SWBLI flows.^{59–61} For the upper wall, a similar saddle-node structure is observed upstream of point A, as the local flow separation has been caused by the first SWBLI [shown in Fig. 9(b)].

The total pressure, P_t , which is an important variable to measure the quality of the internal flow, is shown in Fig. 11. There are two mechanisms for the total pressure loss, the loss of total pressure associated with shock waves, and the friction loss from the boundary layer. The shock wave-induced total pressure loss can be seen as the decrease in P_t when passing through shock-wave in Fig. 11. The local low P_t

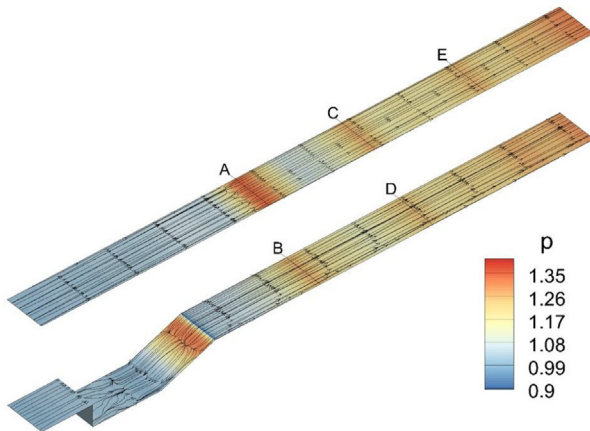


FIG. 10. Wall pressure and skin-friction lines on the upper and lower walls.

zone can be seen around the shock-waves, and it is interesting to note that when the compression waves from the aft wall are focused to form the shock-wave, the related total-pressure loss is also increased.

The vertically averaged total pressure and the total pressure along the central line are plotted in Fig. 12. It can be seen that the total pressure along the central line is maintained at the freestream level, meaning the direct total pressure loss from the shock-wave is negligible. The averaged total pressure, however, shows a clear decreasing trend along the channel. Upstream of the step, a constant total pressure loss rate due to boundary layer is observed. Over the cavity, the averaged total pressure is largely reduced due to the low-energy fluid in the circulation zone. Downstream of the expansion corner, the rate of the total pressure loss is similar to the upstream level, meaning the total pressure loss is still due to the friction inside the boundary layer. Therefore, for the present case, the total pressure loss of the internal flow is mainly contributed from the friction inside the boundary layer, rather than the interaction with shock waves.

The mean velocity and temperature profiles along the representative stations S1–S8 [shown in Fig. 8(a)] are shown in Figs. 13(a) and 13(b), respectively. On the boundary layer attached to the upper wall, we can observe the thickening of the boundary layer due to the SWBLI. The interaction of the shock-wave leads to velocity defect and temperature increase, which can be seen at the S4 and S6 stations. Along the central line of the channel, the decrease in the velocity and increase in temperature as the result of the interaction with shock-wave can be noticed. For the station S2, we can confirm the low-speed

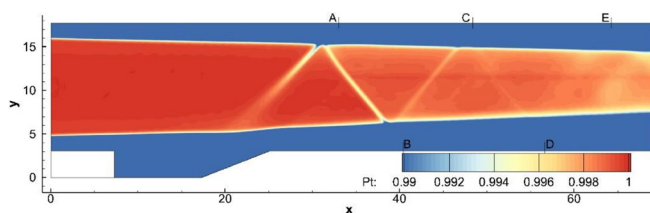


FIG. 11. Total pressure normalized with the free stream total pressure. The legend is scaled for the best view of the total pressure in the central of the channel.

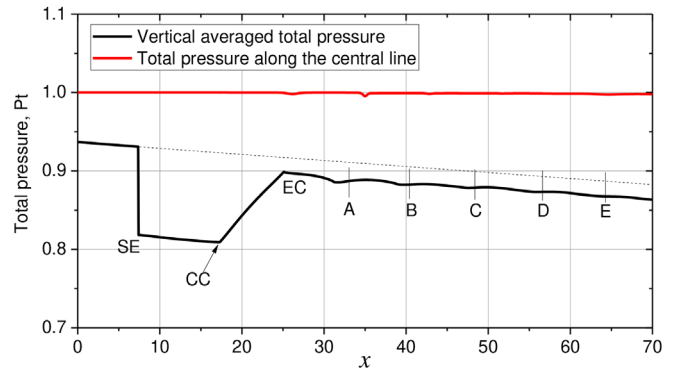


FIG. 12. The vertically averaged total pressure and the total pressure along the central line of the channel ($y = 10.38$). Both quantities are normalized with the freestream total pressure.

and high-temperature fluid in the cavity, and the uniform temperature distribution can be observed in the circulation zone.

D. Reynolds stress

The Reynolds normal stress and turbulence kinetic energy (TKE), $K = \frac{1}{2} \langle u''_i u''_i \rangle$, are shown in Fig. 14, from which we shall note there are several locations where turbulence is locally amplified, especially for the $\langle u'' u'' \rangle$ component. High levels of Reynolds stress and TKE can be seen in the free shear-layer. All the components of the Reynolds normal stress are highly amplified within a short distance downstream of the step edge, where the free shear-layer is being initialized. The reason could be attributed to the strong shear strength. Following the free shear-layer, another high turbulence zone can be identified over the aft wall. This can be attributed to the impingement of the turbulence structures in the shear-layer to the aft wall as shown in Fig. 7. Downstream of the expansion corner, a thick layer with relatively high Reynolds stress is attached to the lower wall, indicating the influence of the free shear-layer to the boundary layer on the lower wall. Around the shock interaction locations, A–E, the turbulence is also locally amplified due to the SWBLI, observed as the local high

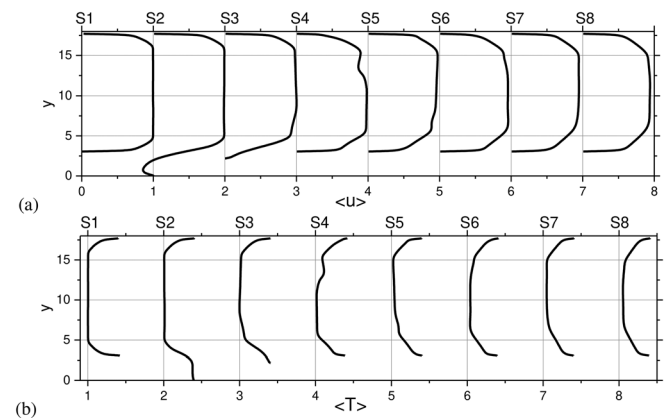


FIG. 13. Mean velocity (a) and temperature (b) profiles on the representative stations. The locations of these stations are shown in Fig. 8(a).

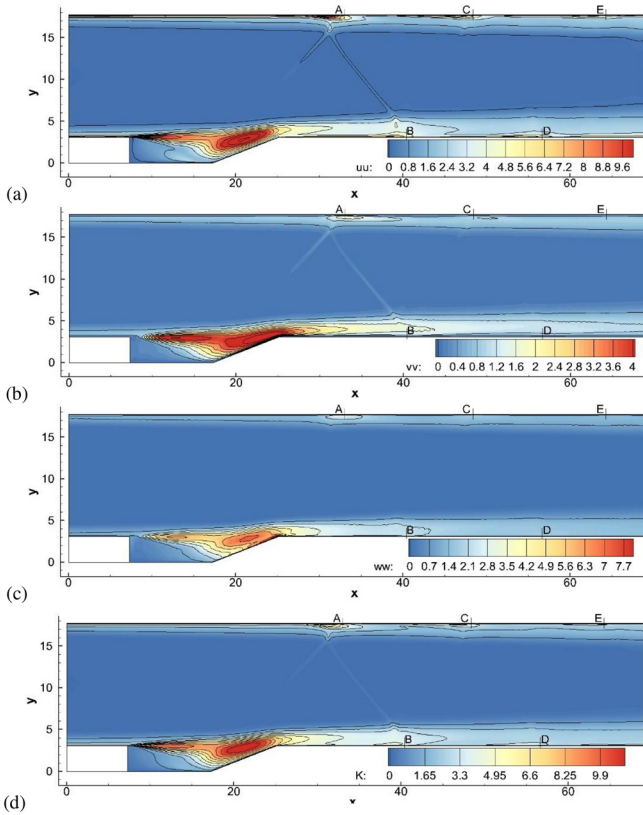


FIG. 14. Reynolds normal stress (a)–(c) and turbulence kinetic energy (d). All quantities are normalized with u_{τ}^2 at the reference location, $x = 5.88$ mm.

value of the Reynolds stress. Through the comparison among different components, the amplification of $\langle u''u'' \rangle$ at all the interaction points is evident, but the amplification of $\langle v''v'' \rangle$ and $\langle w''w'' \rangle$ can only be observed at the point A, where the SWBLI is the strongest. This can be explained by the mechanisms of the turbulence amplification for different components of the Reynolds stress are different, as demonstrated by Fang *et al.*³⁸ However, in the free shear-layer, the behaviors of the different components are observed quite similar.

The profiles of Reynolds normal stress along the representative stations are plotted in Fig. 15, from which we can confirm the high level of turbulence energy in the free shear-layer. $\langle u''u'' \rangle$, $\langle v''v'' \rangle$, and $\langle w''w'' \rangle$ present a similar distribution inside the free shear-layer, indicating the turbulence is more isotropic than wall turbulence.

A double-layer structure can be noticed on the lower half of the $\langle u''u'' \rangle$ profiles at downstream stations in Fig. 15(a). The outer layer is obviously due to the influence of the free shear-layer and the inner layer should be attributed to the regenerated wall turbulence. It is interesting to see that the wall turbulence is regenerated within a short distance downstream of the expansion corner. Near the outlet of the domain, the profiles of Reynolds stress are recovered to equilibrium, although there is still some turbulence energy in the outer layer.

The anisotropy invariant map of the Reynolds stress is further analyzed focusing on the evolution of turbulence in the shear-layer. The invariant map of Lumley and Newman,⁶² namely, the Lumley triangle, uses the coordinate system (Ξ, Ψ) , where

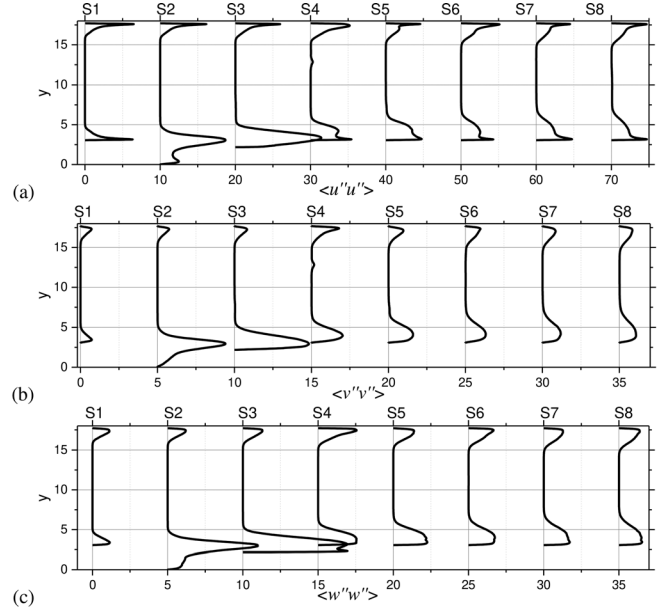


FIG. 15. Profiles of the Reynolds normal stress on the representative stations, (a) $\langle u''u'' \rangle$, (b) $\langle v''v'' \rangle$, and (c) $\langle w''w'' \rangle$. The locations of these stations are shown in Fig. 8(a).

$$\Xi = \sqrt[3]{a_{ij}a_{jm}a_{mi}/6}, \quad \Psi = \sqrt[3]{a_{ij}a_{ij}/6}, \quad (2)$$

and $a_{ij} = \langle u_i''u_j'' \rangle / 2K - \delta_{ij}/3$ is the Reynolds stress anisotropy tensor. The anisotropy of the Reynolds stress evolving along $y = 3.15$ (the corresponding y^+ at the reference location is $y^+ = 15$) from the boundary layer upstream of the cavity to the downstream of the cavity is shown in Fig. 16. It can be seen that the Reynolds stress is close to being axisymmetric with Ξ positive, i.e., the rod-like structure,^{63,64} during the initial formation of the shear-layer. This means the

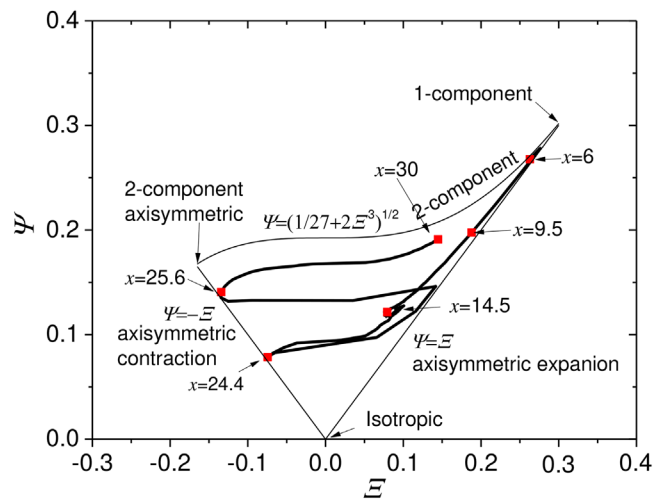


FIG. 16. Evolution of the Lumley triangle of the Reynolds stress anisotropy tensor across the cavity along $y = 3.15$.

characteristic of wall turbulence from the log-layer is still maintained. With the evolution of the shear-layer, the Reynolds stress approaches the $\Psi = -\Xi$ line, indicating the structure is becoming disk-like axisymmetric.⁶⁵ This is the typical characteristic of turbulence around the edge of the mixing layer, where the flow is dominated by free shear.⁶⁶ Around the expansion corner, the Reynolds stress moves rapidly between axisymmetric with $\Psi = \Xi$ and $\Psi = -\Xi$ lines, as the flow structure is expanded and recompressed within a short distance [shown in Fig. 9(a)]. Downstream of the expansion corner, the Reynolds stress is recovering toward the $\Psi = \Xi$ line, indicating the turbulence becomes more anisotropic under the impact of the wall.

The production of TKE is analyzed to explore the amplification of turbulence. According to the previous of Fang *et al.*,³⁸ the production term of turbulence kinetic energy can be decomposed into shear-driven production, P_S , and deceleration production, P_D , as

$$P_K = \underbrace{-\rho \langle u''v'' \rangle \left(\frac{\partial \langle u \rangle}{\partial y} + \frac{\partial \langle v \rangle}{\partial x} \right)}_{P_S} - \underbrace{\rho \langle u''u'' \rangle \frac{\partial \langle u \rangle}{\partial x} - \rho \langle v''v'' \rangle \frac{\partial \langle v \rangle}{\partial x}}_{P_D}. \tag{3}$$

According to the analysis of Fang *et al.*,³⁸ the turbulence amplification in SWBLI is mainly contributed by the deceleration production, although the shear-driven production can last for a long distance in the downstream. The TKE production terms of the present case are shown in Fig. 17, from which we can see the high TKE production in the free shear-layer and around each interaction points. The high TKE production in the free shear-layer has shown two separated zones. The first zone is in the first half of the free shear-layer, from the edge of the

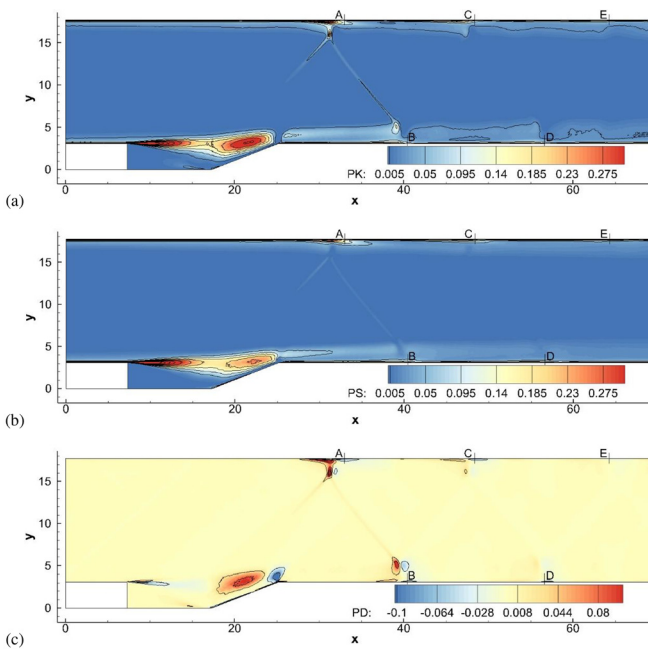


FIG. 17. TKE production (a) and its components: shear production (b) and deceleration production (c). All the quantities are normalized with $\rho_0^2 u_c^4 / \mu_w$ at the reference location.

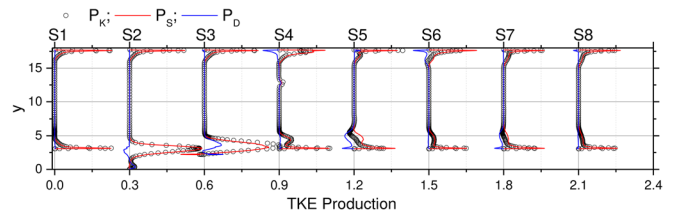


FIG. 18. Profiles of TKE production terms on the selected stations.

step-up to the compression corner, where the TKE production is mainly contributed by the shear production. This is the common characteristics of free shear-layer.⁶⁷ The second zone is above the aft wall, where the turbulence in the shear-layer impinges on the surface of the aft wall. Both the shear production and the deceleration production have non-negligible contributions to the production of turbulence in this zone, meaning the turbulence production here is driven by the shear from the free shear-layer and velocity gradient due to the local strong pressure gradient.

Around the expansion corner, we can observe negative values of P_D due to the annihilation of turbulence by the expansion process. Around each interaction point, we can note a pair of positive and negative P_D zones, as the result of the interaction of the boundary layer with shock-wave and the followed expansion wave. The shear production, P_S , however, plays a minor role around the interaction point, which is consistent with the result in SWBLI.³⁸

The quantitative analysis of the TKE production terms is conducted by comparing the profiles at the selected stations in Fig. 18. At the station S1, the TKE production is entirely contributed by the shear production, as the station is positioned in the zero-pressure-gradient boundary layer. At the station S2, we can see the increase in the production is mainly caused by the growth of the shear production term. At the station S3, the level of the shear production term, P_S , is reduced, compared with P_S on S2, but the total production, P_K , is still increasing. The positive deceleration production, P_D , is the major reason for the growth of P_K . For the following stations, the shear production plays as the major contributor to the generation of TKE. Due to the selected stations that are in the expansion zone of SWBLI, we can note the negatives values of P_D on the stations S4–S8.

E. Pressure fluctuations

The distribution of the root mean square (*rms*) pressure fluctuations, $p_{rms} = \sqrt{\overline{p'p'}}$, is shown in Fig. 19. High p_{rms} can be observed in the cavity region and near the shock-waves. Two separated high p_{rms}

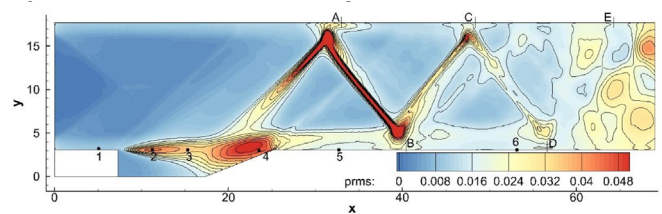


FIG. 19. The *rms* pressure fluctuations normalized with the dynamic pressure of the freestream flow, $q_0 = 0.5\rho_0 u_0^2$. Black dots in (a) mark the locations of probes.

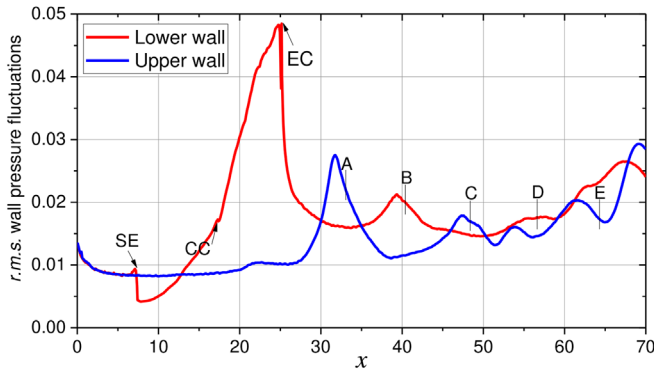


FIG. 20. The *rms* wall pressure fluctuations on the upper and lower walls, normalized with the dynamic pressure of the freestream flow, $q_0 = 0.5\rho_0u_0^2$.

regions can be identified in the cavity region, similar to the observation of Reynolds stress in Fig. 17. The first region is in the core of the free shear-layer, and the strong pressure fluctuations correspond to the instantaneous low-pressure spots shown in Fig. 6(c), which are result of the strong vortical motion of turbulence in the free shear-layer as demonstrated in Fig. 7. The second strong p_{rms} region is seen near the aft wall, and the pressure fluctuations should be attributed to the interaction between the turbulence structures in the shear-layer and the wall.

The strong pressure fluctuations around the shock-waves are the result of the unsteadiness of the shock-waves. It is worth noting the correlation between the intensity of p_{rms} and the strength of shock-

waves reflected in Figs. 6(a) and 6(b), which means a stronger shock-wave causes a higher level of pressure fluctuations. Near the outlet of the computational domain, as the result of the smear of the shock-wave, the distribution of p_{rms} is relatively uniform across the channel.

The profiles of wall pressure fluctuations are plotted in Fig. 20, from which we can see the highest wall pressure fluctuations on the lower wall are reached at the expansion corner, following by a sharp reduction due to the interaction with the expansion fan. Downstream of the expansion corner, local p_{rms} peaks can be identified around each interaction point, indicating the contribution of SWBLI to the local wall pressure fluctuations.

The instantaneous pressure signals recorded on the 6 selected probes (shown in Fig. 19) are presented in Figure 21, in which probe 1 is positioned in the near-wall region of the upstream undisturbed boundary layer; probes 2 and 3 are in the core of the free shear-layer; probe 4 is near the impingement point of the shear-layer; and probes 5 and 6 are in the near-wall region of the downstream boundary layer. The amplification of pressure fluctuations can be clearly observed for the probes in the free shear-layer (2–4), and the signals on these probes also present a low-frequency characteristic. It can be observed that the pressure signals on all the probes reach the statistical steady state after $t = 600 \mu s$, and we analyze the spectral characteristics of the pressure fluctuations from the sampling interval, $t = 600\text{--}1860 \mu s$.

The calculation of the power spectral density (PSD) of the recorded pressure signal, $\phi(\omega)$, is conducted via the method proposed by Choi and Moin,⁶⁸ where $\omega = 2\pi f$ and f is the frequency. The frequency spectrum of the pressure fluctuations at probe 1 is compared with the wall pressure spectrum from an incompressible turbulent channel flow of Choi and Moin⁶⁸ in Fig. 22. A good agreement

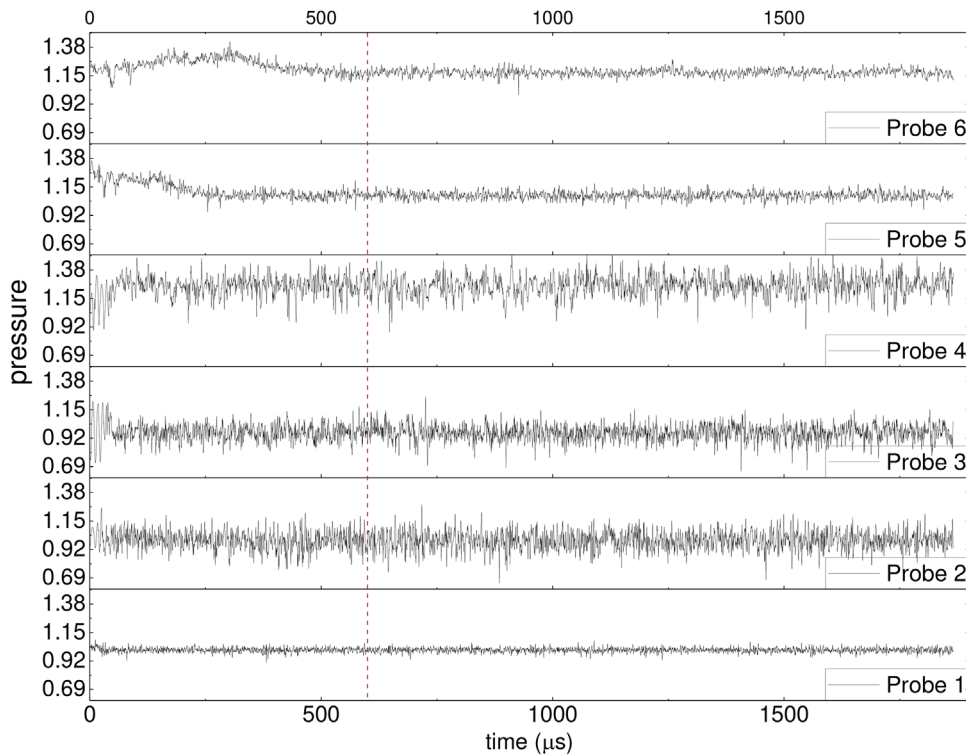


FIG. 21. Pressure signals recorded on the six selected probes. The locations of the probes are shown in Fig. 19. The red dash line marks the location where sampling starts. The pressure is normalized with the freestream pressure.

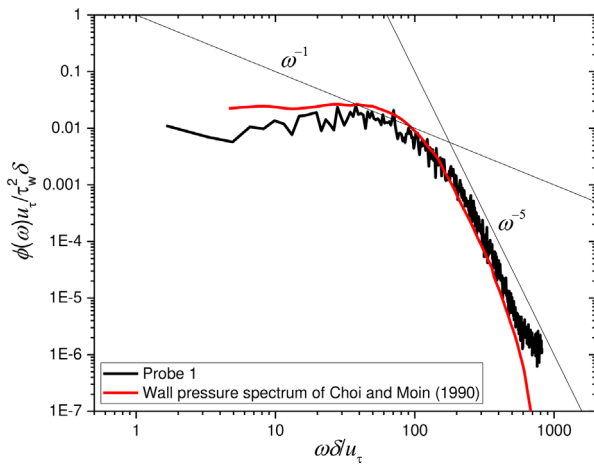


FIG. 22. Comparison of the pressure spectrum at probe 1 with the wall pressure spectrum of Choi and Moin⁶⁸ scaled the local wall units.

between the two spectra can be confirmed at both the low- and high-frequency ends when the local wall units are used to scale ϕ and ω . At the high-frequency end, the spectrum shows a ω^{-5} slope, agreeing with the theoretical prediction of Blake⁶⁹ and Bradshaw.⁷⁰ At the low-frequency end, the intermediate ω^{-1} scaling associated with the turbulent activity in the log layer⁷⁰ can be identified, although the ω^{-1} slope can only be identified within a limited range in Fig. 22 due to the low Reynolds number of the turbulent boundary layer.

The weighted PSD of the pressure signals, $\phi(f)$, from the 6 selected probes is shown in Fig. 23. All the plots are normalized with the local integral value, $\int \phi(f)df$. For probe 1, the most energetic energy is located at $S_t = 0.8$, in which $S_t = f\delta_0/u_0$ is the Strouhal number. This agrees well with the characteristic frequency $f = u_0/\delta_0$ of a supersonic turbulent boundary layer.^{71,72} In the free shear-layer (probes 2–4), broadband low-frequency content can be observed. The peak frequency on probe 2 is at $S_t = 0.68$, close to the characteristic frequency of the incoming turbulent boundary layer. This might be explained as the passing thorough of the large-scale structures from the upstream boundary layer, as the probe 2 is very near the edge of the step. Another spike can be observed at $S_t = 0.19$ (shown as the red circle in Fig. 23), which agrees with the characteristic frequency $S_t = 0.2$ of the vortices due to the Kelvin–Helmholtz (K–H) instability,⁷³ i.e., the shedding of vortices within the shear-layer.⁷² On probe 3, the weighted PSD becomes flatter, with more energy emerging at the low frequencies. The peak frequency moves to $S_t = 0.54$, which could be still attributed to the structures from the upstream boundary layer and a reduced convection mean velocity in the shear-layer. At probe 4, the spectrum keeps being flatter and shifting toward the low-frequency end. The most of the spectral energy is observed within the medium frequency range ($S_t = 0.07$ – 0.5). The peak frequency is identified at $S_t = 0.16$, which is close to the vortex shedding frequency in the shear layer. Therefore, it can be attributed to the landing of the vortical structures in the shear-layer at the mean reattachment point around probe 4. For probe 5, the spectrum moves toward the high-frequency end, with peak frequency identified at $S_t = 0.75$. This clearly indicates the pressure fluctuations are recovering back to the wall turbulence, although there is still a large portion of energy stored

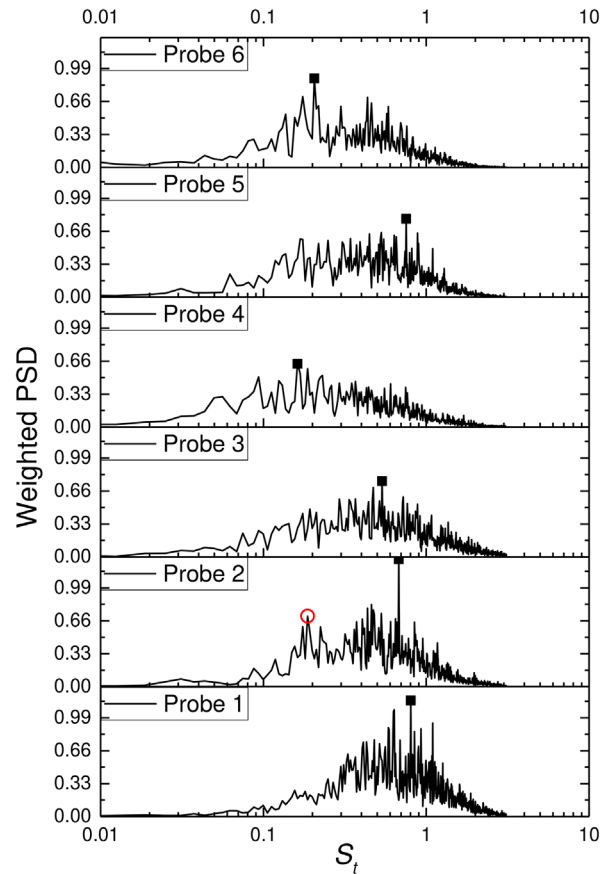


FIG. 23. Weighted PSD of pressure signals against the Strouhal number, S_t . The dots mark the peaks on each curve.

in the low-frequency range. The pressure spectrum at probe 6 presents again a strong low-frequency characteristic, and the peak frequency goes back to $S_t = 0.2$. This is because probe 6 is in the interaction zone by the shock-wave from C to D, as shown in Fig. 19. It is interesting to note the characteristic frequency of the SWBLI is close to the vortex shedding frequency from the shear-layer. This implies the connection between the vortical structures generated in the shear-layer and the downstream SWBLI.

The very low-frequency characteristics ($S_t \sim 0.01$) widely discussed in SWBLI is not observed in the present DNS, which is similar to the result of Hu *et al.*^{72,73} in a supersonic flow over a backward step. They attributed the missing of low-frequency unsteadiness to the separation bubble was more stable in the flow over a backward step. The same mechanism can be also used to explain the present analysis, and the Reynolds number of the present DNS is even lower than the LES of Hu *et al.*,^{72,73} leading to a more stable separation dynamics. It is also possible that the angled aft wall has an ability of stabilizing the shear-layer according to the previous research.⁸ Therefore, the absence of the low-frequency characteristics could be due to the low Reynolds effect and the angled aft wall. Further analysis of the flow at different Reynolds numbers and geometry of the wall should be conducted to clarify this problem.

IV. SUMMARY AND CONCLUSION

The supersonic turbulent flow inside a model scramjet under the cold condition is studied by a DNS approach. The immersed boundary method and a body-fitted mesh are adopted to capture the front and aft walls of the cavity flame-holder, respectively. The DNS data are validated by comparing the mean velocity profile and Reynolds stress in the upstream boundary layer against data from experiment and other DNSs.

The main characteristic of the flow includes a supersonic shear-layer over the cavity and a series of SWBLIs downstream of the cavity. The free shear-layer impinges on the aft wall around the mean reattachment point, which leads to high local pressure and a fan of compression waves. The compression waves merge into a shock-wave and impinge on the upper wall. The shock-wave then reflects between the upper and lower walls, interacting with boundary layers attached to the two walls. High turbulence energy is observed in the shear-layer due to the shear production and K-H instability, and the turbulence is further amplified when the shear-layer impinges on the aft wall. The analysis of the TKE production term indicates the amplification of turbulence in the core of the shear-layer and around the reattachment point is mainly due to the shear production. The flow deceleration mechanism proposed by Fang *et al.*³⁸ mainly presents above the aft wall and around the SWBLI points, where there are strong adverse pressure gradients. The analysis of the pressure signals reveals broadband pressure spectra and a low-frequency characteristics of the shear-layer, similar to the observation in the supersonic flow over a backward step by Hu *et al.*^{72,73} A very low frequency (two orders lower than the boundary layer characteristics frequency) is not observed in the present DNS due to the cavity configuration that confines the separation point and low Reynolds number.

The validation and flow characteristics analysis performed in this study will pave the way for our future studies on this scramjet configuration with detail chemistry reactions. The flow physics revealed near the shear layer and its resulting shock wave above the cavity, where most of the reactions occur, are likely to have a strong impact on the combustion behavior of the scramjet. These topics will be investigated and discussed in the following parts of this work.

ACKNOWLEDGMENTS

This work was supported by the National Science Foundation of China (Grant Nos. 52276096 and 92270203) and the Emerging Interdisciplinary-Young Scholars Project, Peking University, the Fundamental Research Funds for the Central Universities. J.F. also gratefully acknowledges the support of UK Engineering and Physical Sciences Research Council (EPSRC) through the Computational Science Centre for Research Communities (CoSeC) and the UK Turbulence Consortium (Grant No. EP/R029326/1). This work used the ARCHER2 UK National Supercomputing Service (<https://www.archer2.ac.uk>). Part of the numerical simulations was performed on the High Performance Computing Platform of CAPT, Peking University.

AUTHOR DECLARATIONS

Conflict of Interest

The authors have no conflicts to disclose.

Author Contributions

Jian Fang: Conceptualization (equal); Data curation (lead); Formal analysis (lead); Investigation (lead); Methodology (equal); Resources (equal); Software (lead); Validation (lead); Visualization (lead); Writing – original draft (lead). **Xi Deng:** Conceptualization (equal); Methodology (equal); Writing – review & editing (equal). **Zhi X. Chen:** Conceptualization (equal); Funding acquisition (lead); Project administration (lead); Resources (equal); Writing – review & editing (supporting).

DATA AVAILABILITY

The data that support the findings of this study are available from the corresponding author upon reasonable request.

REFERENCES

- A. S. Roudakov, Y. Schikhmann, V. Semenov, P. Novelli, and O. Fourt, "Flight testing of an axisymmetric scramjet—Russian recent advances," in *44th Congress of the International Astronautical Federation (INIST-CNRS, 1993)*, Paper No. 93-S.4.485.
- A. Ben-Yakar and R. K. Hanson, "Cavity flame-holders for ignition and flame stabilization in scramjets: An overview," *J. Propul. Power* **17**, 869 (2001).
- V. A. Vinogradov, S. A. Kobigsky, and M. D. Petrov, "Experimental investigation of kerosene fuel combustion in supersonic flow," *J. Propul. Power* **11**, 130 (1995).
- P. Ortwerth, A. Mathur, V. Vinogradov, V. Grin, M. Goldfeld, and A. Starov, "Experimental and numerical investigation of hydrogen and ethylene combustion in a Mach 3–5 channel with a single injector," AIAA Paper No. 96-3245, 1996.
- M. G. Owens, S. Tehranian, C. Segal, and V. A. Vinogradov, "Flame-holding configurations for kerosene combustion in a Mach 1.8 airflow," *J. Propul. Power* **14**, 456 (1998).
- A. Ben-Yakar and R. Hanson, "Supersonic combustion of cross-flow jets and the influence of cavity flame-holders," AIAA Paper No. 99-0484, 1999.
- A. Ben-Yakar, "Experimental investigation of transverse jets in supersonic crossflows," Ph.D. thesis (Stanford University, 2000).
- X. Zhang, A. Rona, and J. A. Edwards, "The effect of trailing edge geometry on cavity flow oscillation driven by a supersonic shear layer," *Aeronaut. J.* **102**, 129 (2016).
- Z. Wang, H. Wang, and M. Sun, "Review of cavity-stabilized combustion for scramjet applications," *J. Aerosp. Eng.* **228**, 2718 (2014).
- D. L. Davis and R. D. W. Bowersox, "Computational fluid dynamics analysis of cavity flame holders for scramjets," AIAA Paper No. 97-3270, 1997.
- K. M. Kim, S. W. Baek, and C. Y. Han, "Numerical study on supersonic combustion with cavity-based fuel injection," *Int. J. Heat Mass Transfer* **47**, 271 (2004).
- H. B. Ebrahimi and D. V. Gaitonde, "Parametric study of 3D hydrocarbon scramjet engine with cavity," AIAA Paper No. 2007-645, 2007.
- J. Liu, C. J. Tam, T. Lu, and C. Law, "Simulations of cavity-stabilized flames in supersonic flows using reduced chemical kinetic mechanisms," AIAA Paper No. 2006-4862, 2006.
- J. G. Keistler, J. R. L. Gaffrey, X. Xiao, and H. A. Hassan, "Turbulence modeling for scramjet applications," AIAA Paper No. 2005-5382, 2005.
- S. I. Möller, E. Lundgren, and C. Fureby, "Large eddy simulation of unsteady combustion," *Symp. (Int.) Combust.* **26**, 241 (1996).
- M. Boger, D. Veynante, H. Boughanem, and A. Trouvé, "Direct numerical simulation analysis of flame surface density concept for large eddy simulation of turbulent premixed combustion," *Symp. (Int.) Combust.* **27**, 917 (1998).
- P. E. DesJardin and S. H. Frankel, "Large eddy simulation of a nonpremixed reacting jet: Application and assessment of subgrid-scale combustion models," *Phys. Fluids* **10**, 2298 (1998).
- C. Fureby, "Large eddy simulation of combustion instabilities in a jet engine afterburner model," *Combust. Sci. Technol.* **161**, 213 (2000).

- ¹⁹L. Selle, G. Lartigue, T. Poinso, R. Koch, K. U. Schildmacher, W. Krebs, B. Prade, P. Kaufmann, and D. Veynante, "Compressible large eddy simulation of turbulent combustion in complex geometry on unstructured meshes," *Combust. Flame* **137**, 489 (2004).
- ²⁰J. Janicka and A. Sadiki, "Large eddy simulation of turbulent combustion systems," *Proc. Combust. Inst.* **30**, 537 (2005).
- ²¹H. Pitsch, "Large-eddy simulation of turbulent combustion," *Annu. Rev. Fluid Mech.* **38**, 453 (2006).
- ²²H. Wang, Z. Wang, M. Sun, and N. Qin, "Large eddy simulation based studies of jet-cavity interactions in a supersonic flow," *Acta Astronaut.* **93**, 182 (2014).
- ²³M. B. Sun, H. Wang, Z. Wang, H. Geng, J. Liang, W. Liu, and X. Bai, "Experimental and numerical study on flame stabilization in a supersonic combustor with hydrogen injection upstream of cavity flameholders," AIAA Paper No. 2009-5187, 2009.
- ²⁴M. Sun, H. Wu, Z. Fan, H. Wang, X. Bai, Z. Wang, J. Liang, and W. Liu, "Flame stabilization in a supersonic combustor with hydrogen injection upstream of cavity flame holders: Experiments and simulations," *Proc. Inst. Mech. Eng., Part G* **225**, 1351 (2011).
- ²⁵H. Wang, Z. Wang, M. Sun, and N. Qin, "Experimental and numerical investigation of cavity-based supersonic flow and combustion," *Proc. Inst. Mech. Eng., Part G* **228**, 781 (2013).
- ²⁶H. Wang, N. Qin, M. Sun, H. Wu, and Z. Wang, "A hybrid LES (large eddy simulation)/assumed sub-grid PDF (probability density function) model for supersonic turbulent combustion," *Sci. China Technol. Sci.* **54**, 2694 (2011).
- ²⁷K. K. Ramesh, J. R. Edwards, C. P. Goynes, and J. C. McDaniel, "Large eddy simulation of high-speed, premixed ethylene combustion," AIAA Paper No. 2015-0356, 2015.
- ²⁸M. Zhang, Z. Hu, G. He, and P. Liu, "Large-eddy simulation of kerosene spray combustion in a model scramjet chamber," *Proc. Inst. Mech. Eng., Part G* **224**, 949 (2010).
- ²⁹H. Sitaraman, S. Yellapantula, M. T. Henry De Frahan, B. Perry, J. Rood, R. Grout, and M. Day, "Adaptive mesh based combustion simulations of direct fuel injection effects in a supersonic cavity flame-holder," *Combust. Flame* **232**, 111531 (2021).
- ³⁰T. Poinso, S. Candel, and A. Trouvé, "Applications of direct numerical simulation to premixed turbulent combustion," *Prog. Energy Combust.* **21**, 531 (1995).
- ³¹J. H. Chen, "Petascale direct numerical simulation of turbulent combustion—fundamental insights towards predictive models," *Proc. Combust. Inst.* **33**, 99 (2011).
- ³²T. Colonius, "Direct numerical simulation of sound generation in turbulent shear flows," *J. Acoust. Soc. Am.* **105**, 1007 (1999).
- ³³Y. Sun, K. Taira, L. N. Cattafesta, and L. S. Ukeiley, "Global instabilities of compressible open-cavity flows," *J. Fluid Mech.* **826**, 270 (2017).
- ³⁴A. Hamed, D. Basu, A. Mohamed, and K. Das, "Direct numerical simulations of high speed flow over cavity," in Proceedings of the Third AFOSR International Conference on DNS/LES, 2001.
- ³⁵J. Fang, Y. Yao, Z. Li, and L. Lu, "Investigation of low-dissipation monotonicity-preserving scheme for direct numerical simulation of compressible turbulent flows," *Comput. Fluids* **104**, 55 (2014).
- ³⁶J. Fang, Y. Yao, A. A. Zheltovodov, Z. Li, and L. Lu, "Direct numerical simulation of supersonic turbulent flows around a tandem expansion-compression corner," *Phys. Fluids* **12**, 125104 (2015).
- ³⁷J. Fang, Y. Yao, A. A. Zheltovodov, and L. Lu, "Investigation of three-dimensional shock wave/turbulent-boundary-layer interaction initiated by a single fin," *AIAA J.* **55**, 509 (2017).
- ³⁸J. Fang, A. A. Zheltovodov, Y. Yao, C. Moulinec, and D. R. Emerson, "On the turbulence amplification in shock-wave/turbulent boundary layer interaction," *J. Fluid Mech.* **897**, A32 (2020).
- ³⁹J. Fang, Z. Li, and L. Lu, "An optimized low-dissipation monotonicity-preserving scheme for numerical simulations of high-speed turbulent flows," *J. Sci. Comput.* **56**, 67 (2013).
- ⁴⁰S. Gottlieb and C. W. Shu, "Total variation diminishing Runge-Kutta schemes," *Math. Comput.* **67**, 73 (1998).
- ⁴¹R. D. Rockwell, C. P. Goynes, H. Chelliah, J. C. McDaniel, B. E. Rice, J. R. Edwards, L. M. L. Cantu, E. C. A. Gallo, A. D. Cutler, and P. M. Danehy, "Development of a premixed combustion capability for Dual-Mode scramjet experiments," *J. Propul. Power* **34**, 438 (2017).
- ⁴²C. M. Geipel, R. Rockwell, H. Chelliah, A. D. Cutler, C. Spelker, Z. Hashem, and P. M. Danehy, "High-spatial-resolution OH PLIF visualization in a cavity-stabilized ethylene-air turbulent flame," AIAA Paper No. 2017-3901, 2017.
- ⁴³J. W. Kirik, C. P. Goynes, J. C. McDaniel, R. D. Rockwell, L. M. L. Cantu, E. C. A. Gallo, and A. D. Cutler, "Aerodynamic characterization of a cavity flameholder in a premixed dual-mode scramjet," *J. Propul. Power* **34**, 739 (2017).
- ⁴⁴A. D. Cutler, E. C. A. Gallo, L. M. L. Cantu, R. D. Rockwell, and C. P. Goynes, "Coherent anti-Stokes Raman spectroscopy of a premixed ethylene-air flame in a dual-mode scramjet," *Combust. Flame* **189**, 92 (2018).
- ⁴⁵R. F. Johnson, G. B. Goodwin, A. Kercher, A. Corrigan, and H. K. Chelliah, "Discontinuous-Galerkin simulations of premixed ethylene-air combustion in a cavity combustor," AIAA Paper No. 2019-1444, 2019.
- ⁴⁶P. Sagaut, "Theoretical background: Large-eddy simulation," in *Large-Eddy Simulation for Acoustics*, 1st ed. (Cambridge University Press, Cambridge, 2007), pp. 89–127.
- ⁴⁷N. S. Dhamankar, G. A. Blaisdell, and A. S. Lyrintzis, "Overview of turbulent inflow boundary conditions for large-eddy simulations," *AIAA J.* **56**, 1317 (2017).
- ⁴⁸D. H. Rudy and J. C. Strikwerda, "Boundary conditions for subsonic compressible Navier-Stokes calculations," *Comput. Fluids* **9**, 327 (1981).
- ⁴⁹T. J. Poinso and S. K. Lele, "Boundary conditions for direct simulations of compressible viscous flows," *J. Comput. Phys.* **101**, 104 (1992).
- ⁵⁰F. D. Vanna, F. Picano, and E. Benini, "A sharp-interface immersed boundary method for moving objects in compressible viscous flows," *Comput. Fluids* **201**, 104415 (2020).
- ⁵¹S. Pirozzoli and M. Bernardini, "Turbulence in supersonic boundary layers at moderate Reynolds number," *J. Fluid Mech.* **688**, 120 (2011).
- ⁵²L. Murlis, H. M. Tsai, and A. P. Bradshaw, "The structure of turbulent boundary layers at low Reynolds numbers," *J. Fluid Mech.* **122**, 13 (1982).
- ⁵³L. P. Erm and P. N. Joubert, "Low Reynolds number turbulent boundary layers," *J. Fluid Mech.* **230**, 1 (1991).
- ⁵⁴P. R. Spalart, "Direct numerical simulation of a turbulent boundary layer up to $Re_\theta = 1410$," *J. Fluid Mech.* **187**, 61 (1988).
- ⁵⁵L. Duan, I. Beekman, and M. P. Martin, "Direct numerical simulation of hypersonic turbulent boundary layers. III. Effect of Mach number," *J. Fluid Mech.* **672**, 245 (2011).
- ⁵⁶J. Zhou, R. J. Adrian, S. Balachandar, and T. M. Kendall, "Mechanisms for generating coherent packets of hairpin vortices in channel flow," *J. Fluid Mech.* **387**, 353–396 (1999).
- ⁵⁷H. Le, P. Moin, and J. Kim, "Direct numerical simulation of turbulent flow over a backward-facing step," *J. Fluid Mech.* **330**, 349–374 (1997).
- ⁵⁸S. Scharnowski and C. J. Kähler, "Investigation of a transonic separating/reattaching shear layer by means of PIV," *Theor. Appl. Mech. Lett.* **5**, 30–34 (2015).
- ⁵⁹A. A. Zheltovodov, E. Schulein, and V. N. Yakovlev, "Development of turbulent boundary layer under conditions of mixed interaction with shock and expansion waves," in 28–83 *ITAM* (USSR Academy of Sciences, Siberian Branch, Novosibirsk, 1983).
- ⁶⁰A. A. Zheltovodov and V. N. Yakovlev, "Stages of development, flowfield structure and turbulence characteristics of compressible separated flows in the vicinity of 2D obstacles," in 27–86 *ITAM* (USSR Academy of Sciences, Siberian Branch, Novosibirsk, 1986).
- ⁶¹M. S. Loginov, N. A. Adams, and A. A. Zheltovodov, "Large-eddy simulation of shock-wave/turbulent-boundary-layer interaction," *J. Fluid Mech.* **565**, 135–169 (2006).
- ⁶²J. Lumley and G. Newman, "The return to isotropy of homogeneous turbulence," *J. Fluid Mech.* **82**, 161–178 (1977).
- ⁶³M. Emory and G. Iaccarino, "Visualizing turbulence anisotropy in the spatial domain with componentality contours," in *Center for Turbulence Research Annual Research Briefs* (Center for Turbulence Research, 2014), pp. 123–138.
- ⁶⁴M. Jadidi, H. K. Param, A. Revell, and Y. Mahmoudi, "Flow leakage and Kelvin-Helmholtz instability of turbulent flow over porous media," *Phys. Fluids* **34**, 105114 (2022).

- ⁶⁵A. J. Simonsen and P. Å. Krogstad, “Turbulent stress invariant analysis: Clarification of existing terminology,” *Phys. Fluids* **17**, 088103 (2022).
- ⁶⁶S. B. Pope, *Turbulent Flows* (Cambridge University Press, 2001).
- ⁶⁷C. Pantano and S. Sarkar, “A study of compressibility effects in the high-speed turbulent shear layer using direct simulation,” *J. Fluid Mech.* **451**, 329–371 (2002).
- ⁶⁸H. Choi and P. Moin, “On the space-time characteristics of wall-pressure fluctuations,” *Phys. Fluids A* **2**, 1450–1460 (1990).
- ⁶⁹W. K. Blake, *Mechanics of Flow-Induced Sound and Vibration* (Academic Press, London, 1986).
- ⁷⁰P. Bradshaw, “‘Inactive’ motion and pressure fluctuations in turbulent boundary layers,” *J. Fluid Mech.* **30**, 241–258 (1967).
- ⁷¹H. A. L. Kistler, “Fluctuating wall pressure under a separated supersonic flow,” *J. Acoust. Soc. Am.* **36**, 543–550 (1964).
- ⁷²W. Hu, S. Hickel, and B. W. van Oudheusden, “Low-frequency unsteadiness mechanisms in shock wave/turbulent boundary layer interactions over a backward-facing step,” *J. Fluid Mech.* **915**, A107 (2021).
- ⁷³W. Hu, S. Hickel, and B. W. van Oudheusden, “Dynamics of a supersonic transitional flow over a backward-facing step,” *Phys. Rev. Fluids* **4**, 103904 (2019).